Journal of Environmental Chemical Engineering 9 (2021) 106753

Contents lists available at ScienceDirect

Journal of Environmental Chemical Engineering

journal homepage: www.elsevier.com/locate/jece

Porous biochar supported Ag_3PO_4 photocatalyst for "two-in-one" synergistic adsorptive-photocatalytic removal of methylene blue under visible light irradiation

Xiaoqian Wei [a,1], Fang Yu [d,1], Jiawei Ji [b], Yandi Cai [a], Weixin Zou [a,*], Yulin Zheng [c], Jinsheng Huang [c], Yue Zhang [c], Yicheng Yang [c], Mu. Naushad [e], Bin Gao [c], Lin Dong [a]

[a] State Key Laboratory of Pollution Control and Resource Reuse, School of the Environment, Nanjing University, Nanjing 210023, PR China
[b] School of Chemistry and Chemical Engineering, Jiangsu Key Laboratory of Vehicle Emissions Control, Center of Modern Analysis, Nanjing University, Nanjing 210023, PR China
[c] Department of Agricultural and Biological Engineering, University of Florida, Gainesville, FL 32611, United States
[d] School of Resource and Environmental Sciences, Wuhan University, 299 Bayi Road, Wuhan 430072, China
[e] Chemistry Department, College of Sciences, King Saud University, Riyadh 11451, Kingdom of Saudi Arabia

ARTICLE INFO

Editor: Dr. GL Dotto

Keywords:
Porous biochar
Two-in-one synergistic adsorptive-photocatalytic
Photocatalytic methylene blue
Interfacial effect
Reaction mechanism

ABSTRACT

The synergistic adsorption and photocatalysis is of importance to pollutant degradation, and thus the design of both adsorption and photocatalytic sites on one site of the catalyst is worthy of investigation. In the work, a bamboo biochar with rich porous structure was synthesized to support Ag_3PO_4 photocatalyst (AP/PBB) through a ball mill-pyrolysis-precipitation method. Owing to the large surface area of PBB, most of AP nanoparticles were well-dispersed and Ag^0 species were in-situ generated in the preparation, which was beneficial for absorbing more visible light. Furthermore, a stronger interaction, i.e., built-in electric field between AP and PBB was observed, and thus the photo-generated electrons transfer quickly from AP to PBB via the Ag^0 bridge. Furthermore, the transferred electrons reacted with the surface adsorbed oxygen species on PBB to produce ·OH radicals, and then oxidized the methylene blue (MB) molecules on PBB. Therefore, both adsorption and photocatalytic sites on one site, i.e., "two-in-one" of the AP/PBB photocatalyst exhibited higher MB degradation efficiency (95.6%), compared with AP/common biochar. This work affords a novel strategy for biochar-based photocatalysts for effective contaminant removal.

1. Introduction

Due to the rapid development of industrialization and urbanization, water pollution caused by various organic dyes threatens the living environment and health of human beings. Heterogeneous photocatalysis utilizing solar energy is a recognized technology for energy conservation and environmental restoration [1,2]. Therefore, it is imperative to explore and develop visible-light responsive semiconductor-based photocatalytic materials for rapid and efficient removal of organic pollutants. Compared with other carbon materials, biochar (BC) has attracted considerable attention recently owing to its low cost, high porosity, large specific surface area, rich surface functional groups, and good electrochemical property [3]. For example, in BC-based photocatalysts, BC can act as an electron reservoir to promote charge separation and expand the light response range [4]. Furthermore, the electrons transferring from the persistent free radicals of BC to H_2O_2, can produce ·OH and then oxidize organic pollutants [5]. However, most of the pristine BC has limited pore structure and relatively low surface area, leading to low adsorption capacity for macromolecular compounds [6].

The porous BC (PBC) is regarded as a promising advanced carbon material with large surface area, relatively fast diffusion kinetic, high adsorption capacity, and good hydrothermal stability to support semiconductor materials for enhanced adsorption and photocatalytic performances [7]. Ye et al. used the porous graphite BC (PGBC) modifying with graphene-molybdenum disulfide (g-MoS_2) nanosheets, which displays quite high efficiency for tetracycline hydrochloride removal due to

* Corresponding author.
E-mail address: wxzou2016@nju.edu.cn (W. Zou).
[1] Xiaoqian Wei and Fang Yu contributed equally to this work.

https://doi.org/10.1016/j.jece.2021.106753
Received 6 September 2021; Received in revised form 22 October 2021; Accepted 4 November 2021
Available online 11 November 2021
2213-3437/© 2021 Elsevier Ltd. All rights reserved.

the synergy between adsorption and photocatalysis [8]. Due to the excellent conductivity and facilitated mass transport of PGBC, possessed, various techniques have been developed to fabricate PBC including in situ catalysis [9], physical or chemical post-activation [10,11], carbonization of aerogels or cryogels [12], hard or soft template [12] and so on. Among these approaches, hard template synthesis method has been identified as a desirable way to control the pore-size distributions of BC [12]. Recently, our research has found that BC with high specific surface area and rich pore structure can be obtained by MgO hard template method.

Silver phosphate (Ag_3PO_4) is a common semiconductor with a high valence band (VB) potential position, leading to excellent photo-oxidative capabilities for degradation of organic compounds under visible light irradiation [13,14]. However, some disadvantages of pure Ag_3PO_4 limit its practical applications. For example, the crystallite size of Ag_3PO_4 prepared by the traditional method is relatively large (0.5–2 μm), which narrows its response range of visible light [15]. Besides, Ag_3PO_4 has a relatively high Ksp of 1.6×10^{-16} and may slightly dissolute in aqueous solutions, resulting in low activity and structural stability [16]. Even worse, since the conduction band (CB) potential of Ag_3PO_4 (0.45 V) is higher than the hydrogen potential and the photo-generated electrons possess high migration ability during the photocatalytic process, it is easier to encounter photo-corrosion and significantly decrease its photocatalytic efficiency and stability [17,18].

The development of composite and functionalized materials not only improves their surface properties and light absorption ability but also introduces interface effects, making biochar-based materials a promising photocatalyst. [19]. Recently, it has been proposed that carbon materials, such as BC, can effectively improve the photocatalytic performance and stability of Ag_3PO_4 [20–22]. Liu et al. loaded Ag_3PO_4 onto amino-modified BC (AMB) by a facile liquid phase deposition method. The obtained Ag/Ag_3PO_4/AMB composite exhibited much higher photodegradation efficiency of amoxicillin compared with pure Ag_3PO_4 [22]. Talukdar and co-workers successfully synthesized a magentic Z-scheme Ag_3PO_4/Fe_3O_4-activated BC photocatalyst, showing remarkable photodegradation efficiency to bisphenol A under visible-LED-light illumination [23]. Most reports on Ag_3PO_4/biochar materials for adsorption and photodegradation of organic dyes are about the applications and characteristics of the materials. However, porous BC with large surface area, high adsorption capacity, and rich surface adsorbed species is paid little attention in modifying Ag_3PO_4. Besides, heterojunction photocatalysts are very popular due to their fast charge separation efficiency, which is mainly attributed to the formation of a built-in electric field [24–26]. Therefore, the design of both adsorption and photocatalytic sites on one site of the catalyst is worthy of investigation through establishing the built-in electric field.

In this work, we innovatively developed a simple, low cost, and eco-friendly hard template method (ball mill combined with pyrolysis) for preparing porous BC, which obtains abundant pores of nonuniform size to facilitate the distribution and stabilization of Ag_3PO_4 photocatalysts. We pioneered the synthesis of porous bamboo BC (PBB) using the hard template method, which was used to support Ag_3PO_4 to fabricate an Ag_3PO_4/PBB composite photocatalyst (AP/PBB). In addition, the common biochar-based photocatalyst (AP/BB) sample was also prepared. Both of AP/PBB and AP/BB photocatalysts were employed for the removal of model organic contaminant MB to compare their effectiveness and show the advantage of the AP/PBB material. The overarching objectives of this work are as follows: (1) characterize their structural, morphological, physicochemical and photoelectric properties; (2) unveil the roles of the PBB and the structure-performance relationship; (3) evaluate photocatalytic activity and stability of as-synthesized catalysts; (4) clarify the removal mechanism of MB by the AP/PBB photocatalyst.

2. Experimental section

2.1. Catalyst preparation

All reagents were of analytical grade and used without further purification or treatment in this work. Porous bamboo BC was synthesized through the hard-template method. Typically, 1 g MgO and 1 g bamboo biomass powder were mixed and put into a 500 mL agate jar with 200 g balls in a planetary ball mill machine (PQ-N2, USA). The ball milling process was performed in ambient air at 350 rpm for 3 h. The obtained powder material was pyrolysized at 800 °C for 2 h in a tubular furnace and cooled to room temperature under nitrogen flow. Afterwards, it was immersed in 300 mL 1 M HCl solution and stirred for 24 h. Finally, the mesoporous bamboo BC was obtained by washing several times with deionized water and drying at 80 °C overnight. The achieved product was labeled as PBB. Regular bamboo BC without the MgO template was also prepared using the same method and was labeled as BB.

Ag_3PO_4/PBB composite was prepared via in-situ precipitation in dark. Briefly, 0.0858 g PBB and 0.42 g CH_3COOAg were dispersed in 50 mL deionized water by sonicating for 30 min and then keep stir for 24 h. Subsequently, 50 mL 0.1 M Na_3PO_4 was added dropwise into the above suspension and stirred for another 3 h. The collected precipitate was rinsed with deionized water for three times and dried at 60 °C overnight. The as-synthesized sample was denoted as AP/PBB. For comparison, pure Ag_3PO_4 and BB-based composite were prepared under the same conditions and labeled as AP and AP/BB, respectively.

2.2. Catalyst characterization

The surface morphology and microstructure of the photocatalysts were investigated using a field emission scanning electron microscopy (FE-SEM, Nova NanoSEM-450) equipped with a Bruker energy-dispersive X-ray spectroscopy (EDX) elemental mapping analyzer. Transmission electron microscopy (TEM) and high-resolution TEM (HRTEM) images were obtained using a JEM-2100 instrument at an acceleration voltage of 200 kV to study morphologic details and microcrystalline structures of the samples. Surface area and pore structure of the samples were measured through N_2-adsorption at 77 K (Micrometrics ASAP-2020). To identify the crystallographic structures of the materials, X-ray powder diffraction (XRD) analysis was conducted using a Philips X′Pert Pro diffractometer with Ni-filtered Cu Kα radiation ($\lambda = 0.15418$ nm). Surface chemical compositions and electronic states of the as-prepared samples were analyzed by X-ray photoelectron spectroscopy (XPS) analysis using a PHI 5000 Versa Probe high performance electron spectrometer with an Al Kα radiation (1486.6 eV) achromatic X-ray source. The carbonaceous C 1 s line at 284.6 eV was used as reference to calibrate all binding energies. This reference has experimental errors within ±0.1 eV. Fourier transform infrared (FT-IR) spectra were acquired using a Nicolet 5700 FT-IR spectrometer in the range of 400–4000 cm^{-1} with the spectral resolution of 4 cm^{-1}. Raman spectra were recorded by a LabRAM Aramis instrument equipped with an Ar^+ laser beam. Optical absorption properties of the samples were examined using a UV–vis diffuse reflectance spectrophotometer with the reference of $BaSO_4$ (UV-2401, Shimadzu). Photoluminescence (PL) spectra were collected using a FluroMax-4 fluorescence spectrophotometer at room temperature, and the wavelength of the excitation light was 325 nm. The experiments were performed in the solid state. The slit in all measurements was 1.5 nm. spectra were acquired from lines. The electron spin resonance (ESR) measurements were obtained on a JES FA200, JEOL Co. spectrometer with the 5,5-dimethyl-1-pyrroline-N-oxide (DMPO) solvent.

The photoelectrochemical measurements were carried out on a CHI660E electrochemical workstation system adopting a standard three-electrode cell. The photocatalytic materials were deposited on fluorine-doped Tin Oxide (FTO) serve as the working electrode, with a platinum wire and Ag/AgCl electrode as the counter and reference electrodes,

respectively. Na_2SO_4 (0.1 M) was as electrolyte solution and a Xe arc lamp as a light source. The transient photocurrent response was performed at 0.5 V versus Ag/AgCl during the on-off cycles of illumination. Electrochemical impedance spectroscopy (EIS) was tested at −0.6 V (vs. Ag/AgCl) from 10^5 to 0.1 Hz with a modulation amplitude of 20 mV.

2.3. Evaluation of photocatalytic activity

The photodegradation of MB were carried out under visible light irradiation under a 280 W Xe lamp ($\lambda > 400$ nm). 0.05 g of the prepared photocatalysts (dosage of 0.5 g L^{-1}) were placed into a 250 mL quartz vessel containing 100 mL of 40 mg L^{-1} MB solutions. The suspensions were first sonicated for 5 min and then magnetically stirred in dark for 30 min to reach the establishment of an adsorption–desorption equilibrium. During the visible light irradiation, 3 mL of the solution were withdrawn and filtered through 0.22 μm pore size nylon membrane filters for analysis at 10 min intervals. The concentrations of MB filtrates were analyzed with a UV-Vis spectrophotometer at 664 nm.

3. Results and discussion

3.1. Specific surface area and dispersibility

The information on the surface area and pore textures was obtained from the 77 K nitrogen adsorption-desorption analysis. The N_2 adsorption-desorption isotherms classification (Fig. 1a) of PBB and AP/PBB were similar and belonged to type I/IV of the referred IUPAC [27]. The adsorption branch of isotherms tended to increase abruptly under low relative pressures, manifesting the formation of numerous micropores. The hysteresis loops displayed a typical type H3 in the wide range of 0.43–0.99 P/P_0, indicating the existence of a certain number of mesopores and macropores. However, the isotherm of BB and AP/BB were close to type I, corresponding to well-developed microporous structure. The pore size distribution results (Fig. 1b) well support our conclusion. The values summarized in Table 1 show that the BET surface area (117.63 $m^2\ g^{-1}$), the total pore volume (0.139 $cm^3\ g^{-1}$) as well as the mesopore and macropore volume (0.108 $cm^3\ g^{-1}$) of AP/PBB were much larger than that of AP/BB (16.59 $m^2\ g^{-1}$, 0.019 $cm^3\ g^{-1}$ and 0.012 $cm^3\ g^{-1}$, respectively) due to the introduction of the high specific surface area and rich porosity of PBB. Such high surface area and plentiful

Table 1
Surface area and pore properties of the samples.

Samples	S_{BET} ($m^2\ g^{-1}$)	S_{mic} ($m^2\ g^{-1}$)	V_{total} ($cm^3\ g^{-1}$)	V_{mic} ($cm^3\ g^{-1}$)	$V_{mes}+V_{mac}$ ($cm^3\ g^{-1}$)
AP	6	–	–	–	–
AP/BB	16.59	15.11	0.019	0.007	0.012
BB	136.07	113.61	0.103	0.045	0.058
AP/PBB	117.63	74.06	0.139	0.031	0.108
PBB	779.20	554.78	0.864	0.226	0.638

S_{BET}: the total specific surface area was derived from the BET method.
S_{mic}: the micropore surface area was determined by t-Plot method.
V_{total}: the total pore volume was measured at $P/P_0 = 0.99$.
V_{mic}: the micropore volume was analyzed by t-Plot method.
$V_{mes}+V_{mac}$: the mesopore and macropore volume was calculated by V_{total} - V_{mic}.

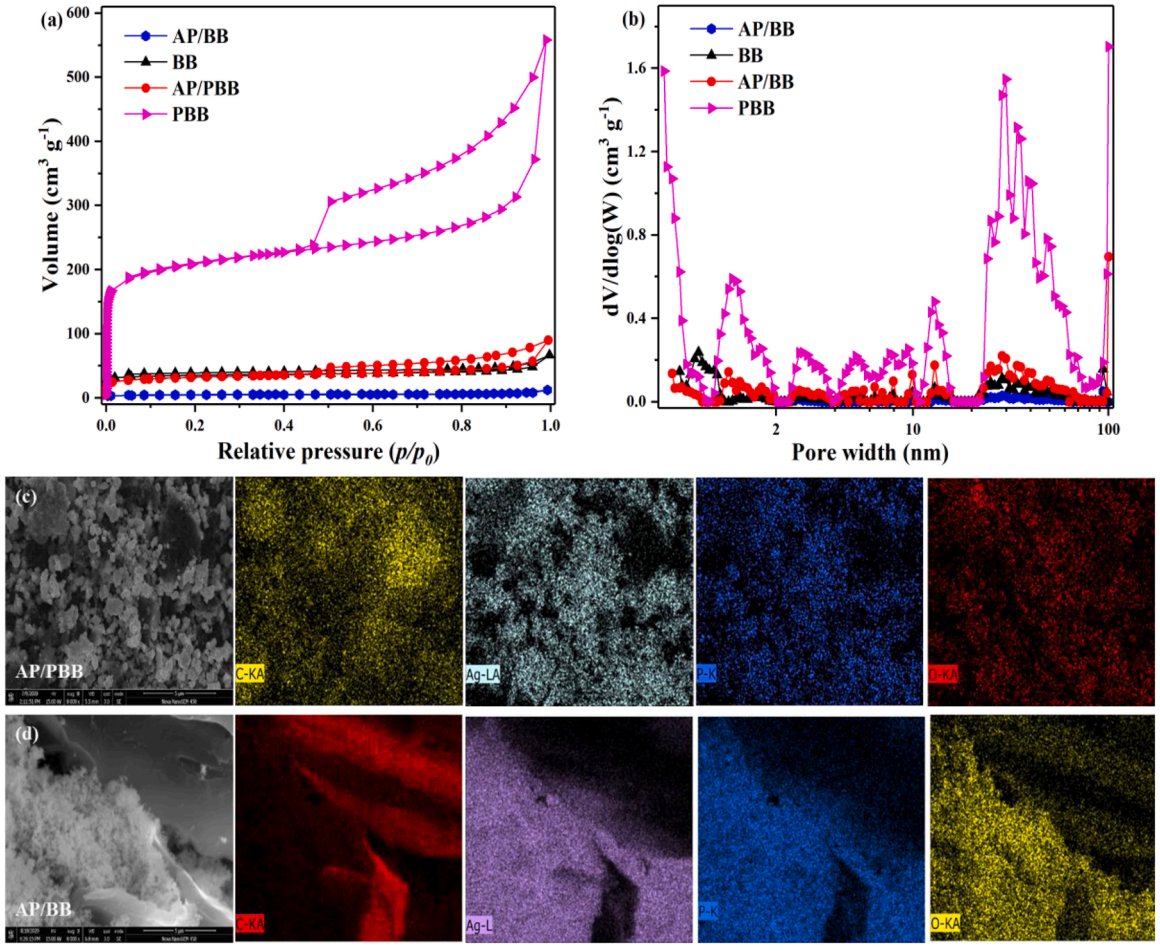

Fig. 1. (a) The N_2 adsorption-desorption isotherms and (b) the corresponding pore-size distribution curve of the AP/BB, BB, AP/PBB and PBB samples. SEM images and EDX elemental mapping of (c) AP/PBB and (d) AP/BB.

pore structure for AP/PBB sample may offer abundant active sites for efficient adsorption and photocatalysis of pollutants and high density of charge diffusion pathways for migration and separation of photogenerated carriers.

The SEM and TEM were applied to further validate morphologic and microstructural details of the obtained materials. The common BB depicted a rough and irregular structure (Fig. S1a, Supporting Information), while the PBB was composed of hollow and thin-walled sphere-like grains with plentiful inhomogeneous size pores (Fig. S1b) revealing that the hard template method (ball mill combined with pyrolysis) was feasible and promising for the synthesis of porous carbon. As expected, the SEM diagram and EDX elemental mapping of AP/PBB hybrid (Fig. 1c) clearly show that irregular AP particles were uniformly dispersed on the surface of PBB, attributing to its large specific surface area and porosity. However, for AP/BB sample (Fig. 1d), most of AP particles were aggregated on the BB, leading to poor photocatalytic activity. Compared with AP/BB, the majority of AP particles could enter the pores of PBB in the AP/PBB composite (Fig. S1c). In addition, the characteristic fringe spacing of 0.27 nm in HRTEM image of AP/PBB (Fig. S1d) is consistent with the (210) lattice plane of Ag_3PO_4 crystal [13].

On the basis of the aforementioned results, we conclude that the as-prepared PBB by the novel hard template technology is a good host to support the dispersion of semiconductor particles to increase active sites.

3.2. Ag^0 species generation and the interface interaction

As shown in Fig. 2a, all observed diffraction peaks of bare AP perfectly match cubic Ag_3PO_4 (JCPDS card No. 06-0505) [28]. In addition to the standard peaks of Ag_3PO_4, several peaks at 38.2°, 44.4°, 64.5° and 77.5° indexed to metallic Ag (JCPDS card No. 04-0783) appear in the AP/BB and AP/PBB spectra. This indicates the presence of metallic Ag on the composites, which may be due to the reduction of Ag ions by BC [21,29]. Generally, the surface plasmon resonance (SPR) effect of Ag particles can increase the utilization rate of light to improve the photocatalytic performance. Compared with that of AP/BB, the intensity of the peaks ascribed to Ag in the AP/PBB composite dramatically enhanced, manifesting higher Ag crystallinity, which suggests that more intensive interaction on AP/PBB interface results in Ag^0 species and thus available visible light is absorbed.

The UV–vis DRS (Fig. 2b) of the synthesized samples were determined to show the light adsorption. It is obviously revealed that AP/PBB composite possessed the strongest optical absorption and significantly extended visible light absorption range with respect to AP and AP/BB. This can be ascribed to the modification of black PBB and the SPR effect of metallic Ag particles of AP/PBB [8,30]. The result also indicates that the synergistic effect of Ag_3PO_4 and PBB may enhance solar energy efficiently to produce more photogenerated electron-hole pairs during the photocatalysis. Subsequently, the PL and transient photocurrent response techniques were introduced to explore the recombination, separation and migration behavior of photogenerated carriers in the as-fabricated photocatalysts. As illustrated in Fig. 2c, the AP/PBB

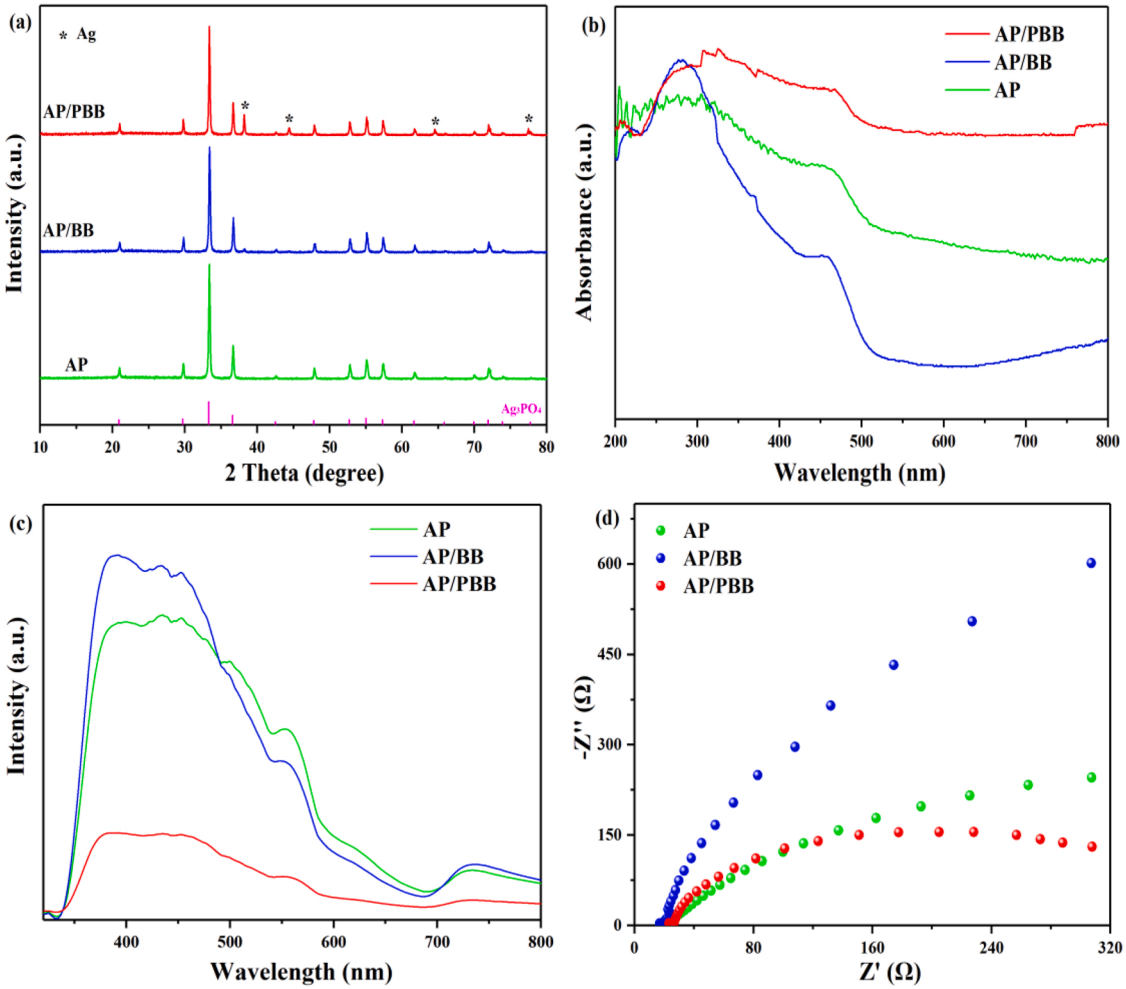

Fig. 2. (a) XRD patterns, (b) UV–Vis DRS, (c) PL spectra and (d) EIS Nyquist plots of AP, AP/BB and AP/PBB samples.

exhibited an extremely weak PL emission signal meaning low recombination rate of the excited charge, suggesting prolonged carrier lifetime. Meanwhile, the photocurrent response intensity of AP/PBB was distinctly higher than that of AP and AP/BB (Fig. S2), implying that PBB plays a crucial role in enhancing the separation and transfer efficiency of charge carriers. In addition, based on the Nyquist plots (Fig. 2d), the charge transfer resistance of the photocatalysts followed the order of AP/PBB < AP < AP/BB, indicating Ag_3PO_4 anchored on the surface of PBB can greatly raise conductivity and accelerate electron transfer. All these photoelectric characterization results demonstrate that because of the larger surface area and richer pore textures of PBB, more intensive interactions are present on AP/PBB interface, leading to Ag^0 species generation, visible light absorption, and photo-generated charge separation.

Furthermore, the detailed information about chemical compositions and states, as well as the interfacial electronic effect of the as-prepared samples were revealed by XPS. In the Ag 3d spectra (Fig. 3a), the two peaks (374.5 and 368.5 eV) related to metallic Ag were discerned from the spectra of AP/BB and AP/PBB [17]. As expected, more Ag^0 were formed in the AP/PBB (49.2%) compared with AP/BB (47.1%) during the synthesis of the composites, which can be attributed to the higher adsorption capacity of porous BC for Ag^+. The formation of metallic Ag can expand light absorption range duo to the SPR effect, meanwhile act as a bridge for charge transmission. The other two characteristic peaks of Ag $3d_{5/2}$ and Ag $3d_{3/2}$ orbit located at 367.9 and 374.0 eV are assigned to Ag^+ of Ag_3PO_4 [17]. Interestingly, the two peaks of AP/BB (0.1–0.2 eV) and AP/PBB (0.5–0.6 eV) both shifted toward the lower binding energy, suggesting that the stronger interaction is presented on the AP/PBB composite.

In addition, in comparison with AP/BB, the binding energies of O 1s (Fig. 3b) and P 2p (Fig. 3c) peaks of AP/PBB are also suggested more intensive interfacial effect. The peaks of the O 1s spectra at 530.2, 530.8 and 532.5 eV are exclusively associated with the bulk lattice oxygen and surface oxygen of Ag_3PO_4 as well as the chemisorbed oxygen (–OH/H_2O) [31,32], and the P 2p peak was centered near at 132.5 eV, corresponded to the PO_4^{3-} [33]. In comparison with AP, the binding energies of O 1s and P 2p peaks of AP/BB did not change, whereas these peaks of AP/PBB shifted slightly to lower values, reflecting the close contact and strong interfacial interaction between PBB and AP in the AP/PBB. Therefore, the more obvious shifted binding energies of Ag 3d, O 1s and P 2p on AP/PBB show that stronger built-in electric field is formed on the AP/PBB interface, i.e., higher electron density is present on AP and less electron density is present on PBB.

The surface oxygen-containing function groups were determined. In the O 1s spectra (Fig. 3b), the content rations of the chemisorbed oxygen for AP/PBB (43.6%) and AP/BB (26.9%) were calculated, respectively. On the basis of the report [34], AP/PBB has stronger tendency to adsorb and activate reactant molecules than AP/BB. The C 1s spectra (Fig. 3d) of the as-synthesized samples illustrated three identical peaks located at 284.0 eV (the sp^2 hybridized carbon), 284.6 eV (the adventitious carbon) and 285.3–285.7 eV (the sp^3 hybridized carbon) [35]. In addition, the peak at 288.8 eV for AP/PBB represented carboxyl groups (COOH), while the AP/BB showed the peaks around 286.7 eV ascribed to C-OH/C-O-C [36]. In the FT-IR spectra (Fig. S3), a small adsorption peak

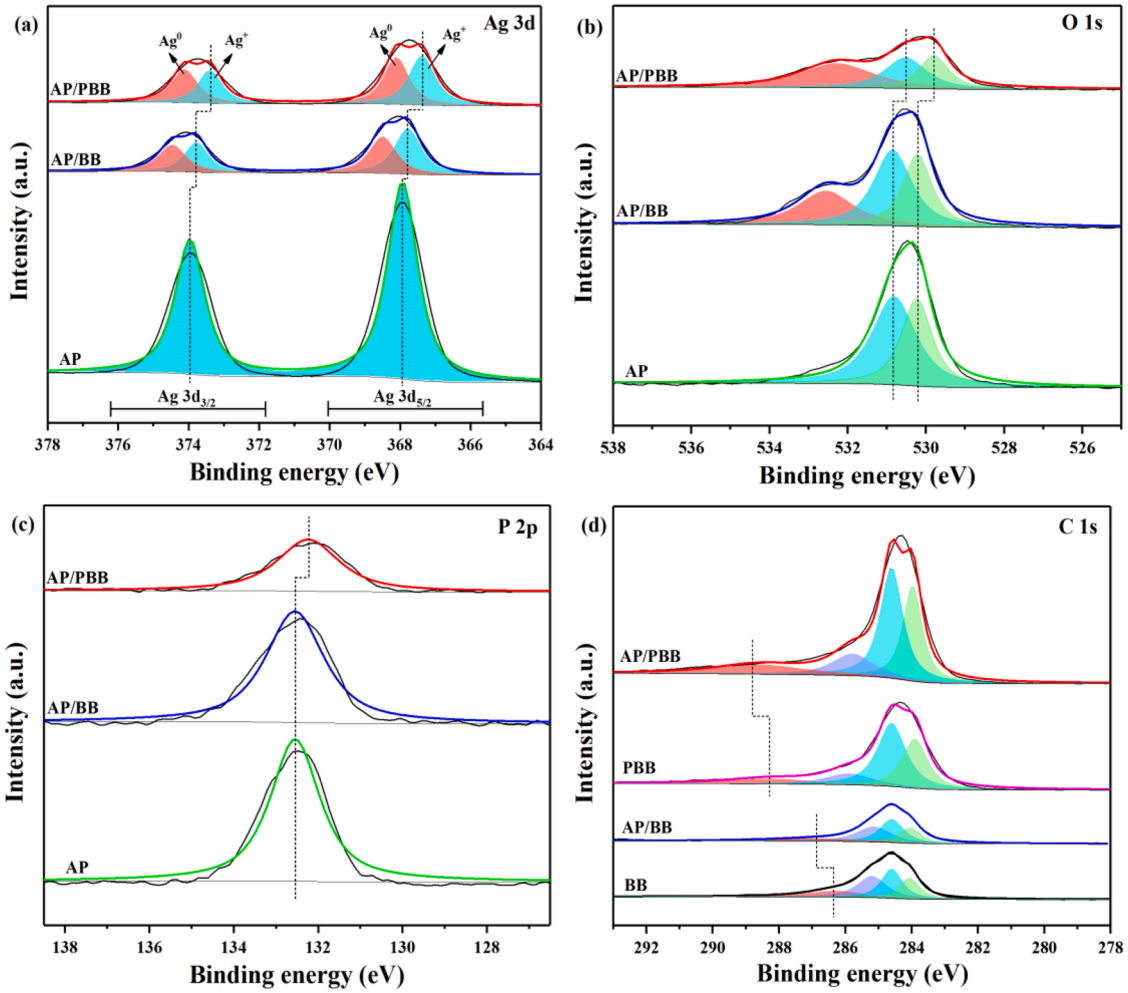

Fig. 3. XPS spectra of the samples: (a) Ag 3d, (b) O 1s, (c) P 2p and (d) C 1s.

located at ~1578 cm^{-1} is related to vibration of the aromatic C═C and carbonyl C═O band in the AP/PBB, whereas it is not detected in the AP/BB [23]. Generally, the carboxyl group is more beneficial for active free radicals generation [37]. On the basis of that, it could be concluded that because of the advantageous structure of PBB, more oxygen-containing species were adsorbed on AP/PBB, which might be helpful for the formation of active free radicals to oxidize MB pollutant.

3.3. Photocatalytic performance and photogenerated free radicals

The photocatalytic performance of the prepared samples was evaluated towards the degradation of MB in aqueous solutions (40 mg L^{-1}) under visible light irradiation (λ > 400 nm). Prior to irradiation, the adsorption of MB onto AP/PBB, AP/BB and AP was assessed in the dark chamber. The results (Fig. 4a) show that all samples achieved the adsorption–desorption equilibrium state within 30 min in the dark. AP/PBB had the highest MB sorption capacity (31.6 mg g^{-1}) compared to pure AP (4.0 mg g^{-1}) and AP/BB (6.0 mg g^{-1}), suggesting PBB may contribute greatly to the sorption of MB. The higher adsorption capacity of AP/PBB may increase the contact between MB and photocatalyst and thus enhance photocatalytic decontamination. As depicted in Fig. 4b, only 19.6% of MB was photodegraded in the blank experiment (without any catalysts), indicating that MB has slight self-degradation ability under visible light irradiation. In contrast, the AP/PBB catalyst strikingly degraded about 95.6% of MB after 1 h of irradiation, demonstrating excellent photocatalytic activity (Table S1). It should be noted that the degradation rate of AP/BB sample (41.1%) to MB was the lowest among the samples, even lower than that of bare AP (55.7%). These clearly demonstrate that PBB is more effective than BB in supporting the photocatalyst, likely because of the mesoporous nature and surface area of PBB. The advantages of PBB are beneficial for in-built electronic field generation, photo-charge transfer, visible light absorption, and active free radical formation.

Expectedly, the variation of the pseudo-first-order rate constants was in agreement with that of photocatalytic activity (Fig. 4c). AP/PBB presented the highest photodegradation rate constant (0.023 min^{-1}, R^2 = 0.999), almost twice and four times of that of AP (0.012 min^{-1}, R^2 = 0.968) and AP/~~P~~BB (0.006 min^{-1}, R^2 = 0.925), respectively. The circulating test of MB degradation was performed to conform the photocatalytic reusability and stability of AP/PBB composite (Fig. 4d). Comparing the results of AP and AP/PBB, it can be found that downward trend of MB degradation efficiency of AP/PBB was slightly improved after three cycles. This is probably due to the formed in-built electronic field, less electronic density is on PBB, which can accept photoinduced electrons formed in the conduction band of AP through the medium Ag, in order to suppress the photo-corrosion. Furthermore, XRD pattern of AP/PBB changed little after the transient photocurrent experiment (Fig. S4) indicating the good photocatalytic stability of AP/PBB composite. These results illustrate that PBB played the core role in accelerating the adsorption and photocatalysis of MB as well as enhancing the

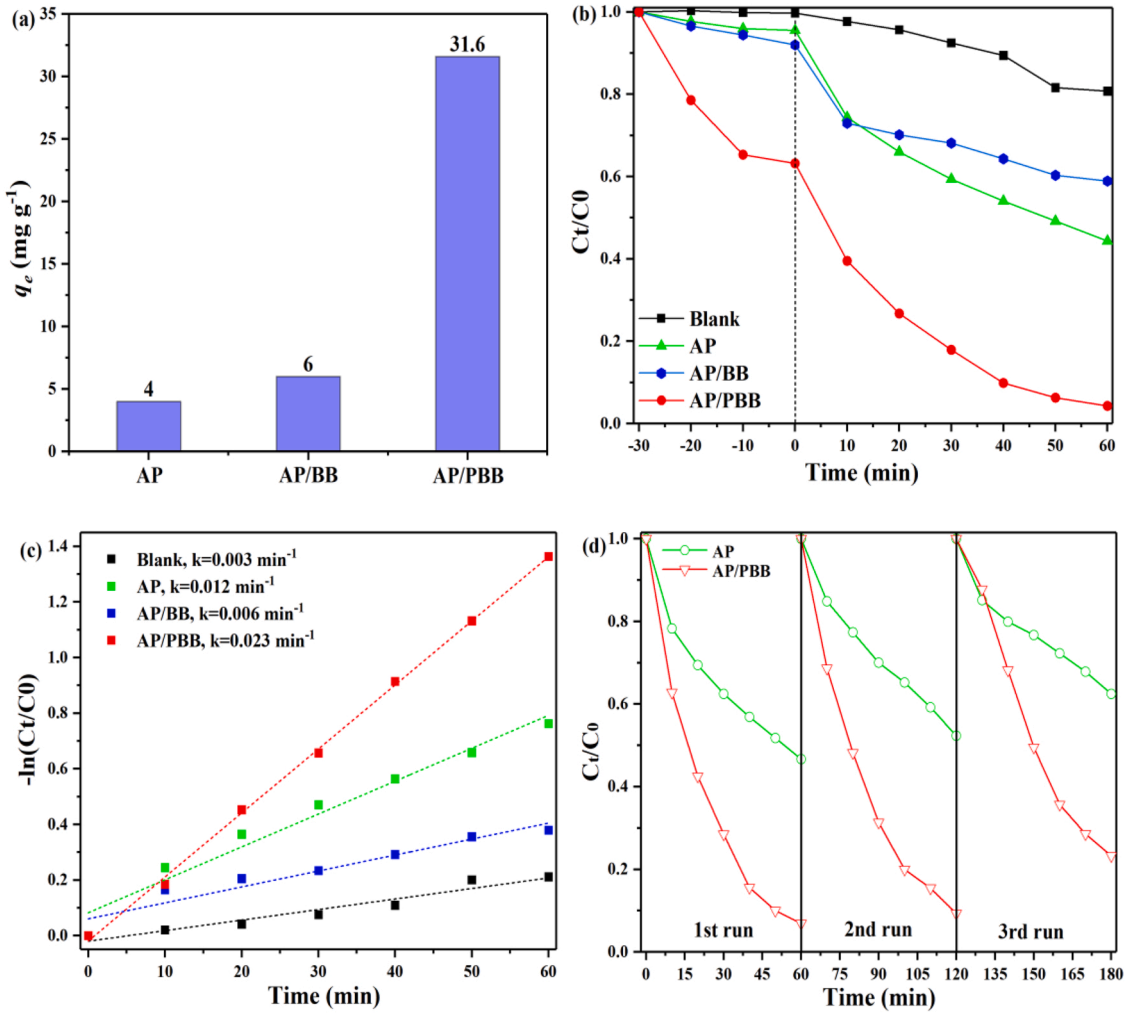

Fig. 4. (a) MB sorption onto the AP, AP/BB and AP/PBB samples and (b-d) MB degradation by the samples under visible light (λ > 400 nm): (b) Photocatalytic activities and (c) linear fits of the photodegradation kinetics, and (d) recyclability of AP, AP/BB and AP/PBB.

photostability.

As is generally known, the active radical species are extremely important and involved in the photodegradation process, and thus the photo-generated active free radicals were determined. The radical trapping experiment using IPA, BQ and EDTA as the effective scavengers of ·OH, $\cdot O_2^-$ and h^+, respectively, was performed over the AP/PBB photocatalyst under visible light irradiation (Fig. 5a). The result show that h^+ and ·OH were the predominant active species in this photocatalytic oxidation process. To further elucidate the considerable MB removal efficiency of AP/PBB, comparison of the ESR spectra is provided in Fig. 5b. Notably, the signal intensity in the system of AP/PBB was much stronger than that of AP/BB indicating its abundant photoactive surface oxygen species, which was attributed to the generation of more photogenerated carriers and the lower recombination of charge carriers under visible light irradiation [38]. The photo-electrons generating on AP were transferred to PBB, and then attacked to the surface adsorbed oxygen species on PBB to produce more ·OH under light irradiation [39]. Finally, the active ·OH radicals effectively oxidized the adsorbed MB pollutant to CO_2 and H_2O.

It is reported that the generation of active free radical species is also related to the defect of BC. Therefore, we carried out the Raman test to confirm defect information of the obtained materials. The Raman spectroscopy (Fig. 5c) of AP/PBB and AP/BB display the peaks in the 1000–1800 cm^{-1} region from the well-documented BC and the two peaks near at 547 and 913 cm^{-1} from the typical Ag_3PO_4 [20,40]. Furthermore, the peaks from 1000 cm^{-1} to 1800 cm^{-1} were fitted to the five peaks C (the CH_3 group), S (adjacent heteroatom defects), D (local defects and disorder), A_1 (5-membered rings) and G (graphitic) by the least-squared method (Fig. 5d) and the fitted values are summarized in Table 2 [40,41]. The relative intensity related to defects (I_S/I_G and I_D/I_G) of AP/PBB were higher than that of AP/BB, indicating AP/PBB can provide more catalytic active sites and trap photogenerated electrons for active free radicals generation [42].

3.4. Possible photocatalytic mechanism

The band structure of the synthesized AP sample was determined using UV–vis DRS and VB XPS. Based on the Kubelka-Munk function, the calculated band gap energy (Eg) value of AP was about 1.99 eV (Fig. S5a). Fig. S5b depicts the VB position for AP was located at 2.60 eV, suggesting it can convert H_2O/OH^- to·OH due to the more positive position than $OH^-/\cdot OH$ potential (+1.99 eV vs. NHE) and $H_2O/\cdot OH$ (+2.38 eV vs. NHE) [43]. Therefore, the CB value of AP reckoned up to be 0.61 eV ($E_{CB} = E_{VB}$-Eg) was more positive than the standard redox potential of $O_2/\cdot O_2^-$ (−0.046 eV vs. NHE), elucidating the absence of $\cdot O_2^-$ in the process of photodegradation of MB by AP/PBB catalyst [43]. Therefore, combined the activity result, AP/PBB had the best performance, owing to more $\cdot O_2^-$ radicals from AP and PBB.

The synergistic mechanism between Ag_3PO_4 and porous BC for efficient removal of MB is illustrated in Fig. 6. (1) When AP/PBB photocatalyst is exposed to the visible light, AP with moderate Eg value can be rapidly excited and generates photoinduced electron-hole pairs. (2)

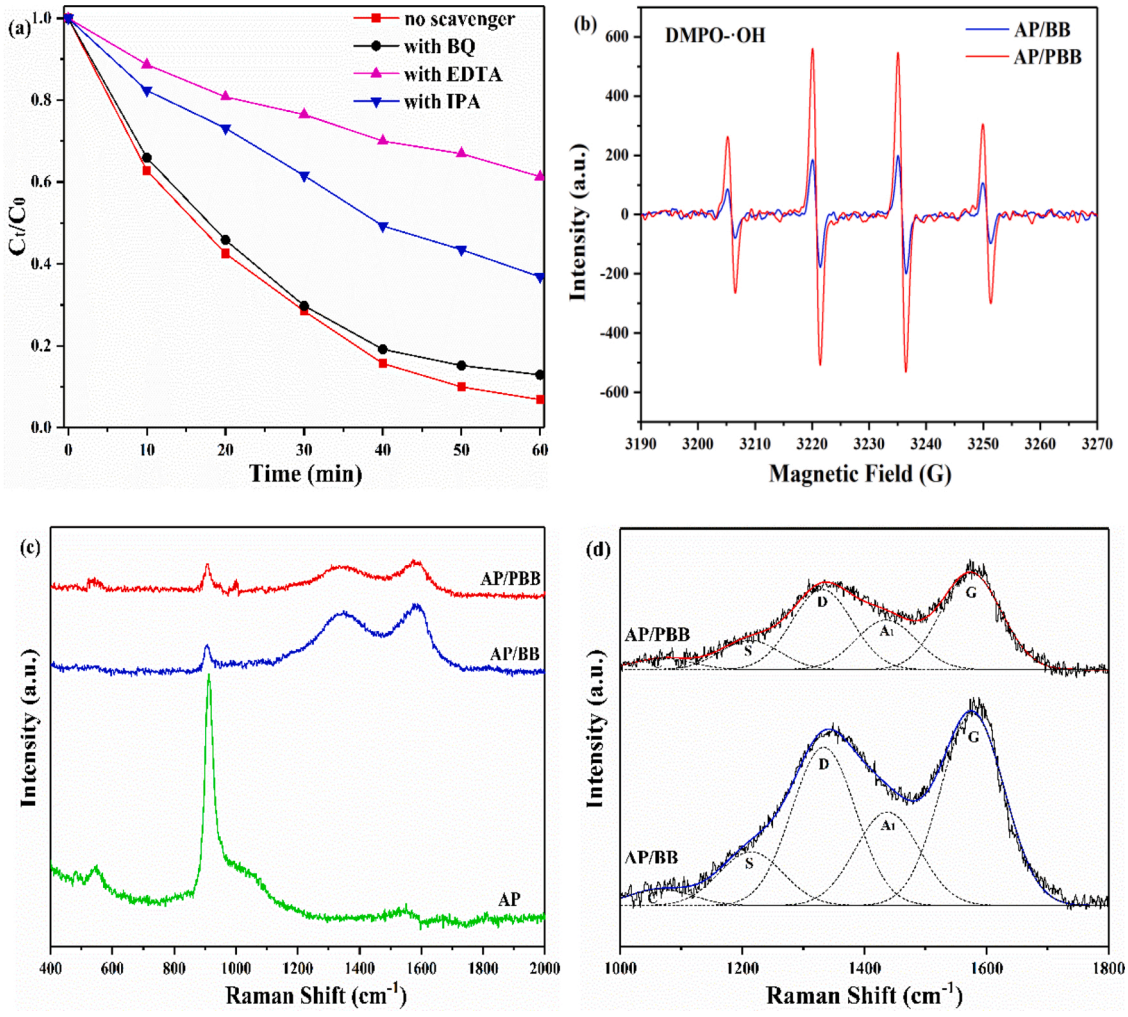

Fig. 5. (a) Effect of scavengers on photocatalytic activity of AP/PBB sample; (b) ESR spectra of AP/BB and AP/PBB in aqueous dispersion for DMPO-·OH under visible light irradiation; (c) Raman spectra of AP, AP/BB and AP/PBB; (d) the enlarged Raman spectra of AP/BB and AP/PBB.

Table 2
The fitted parameters of the enlarged Raman spectra.

Sample	P_C	I_C	P_S	I_S	P_D	I_D	P_{A1}	I_{A1}	P_G	I_G	I_C/I_G	I_S/I_G	I_D/I_G	I_{A1}/I_G
AP/BB	1066	8.1	1214	26.4	1333	77.7	1438	45.9	1577	94.2	0.09	0.28	0.82	0.49
AP/PBB	1070	5.6	1212	14.6	1331	39.4	1435	24.4	1575	47.4	0.12	0.31	0.83	0.51

Note: P refers to position (cm^{-1}), and *I* refers to intensity.

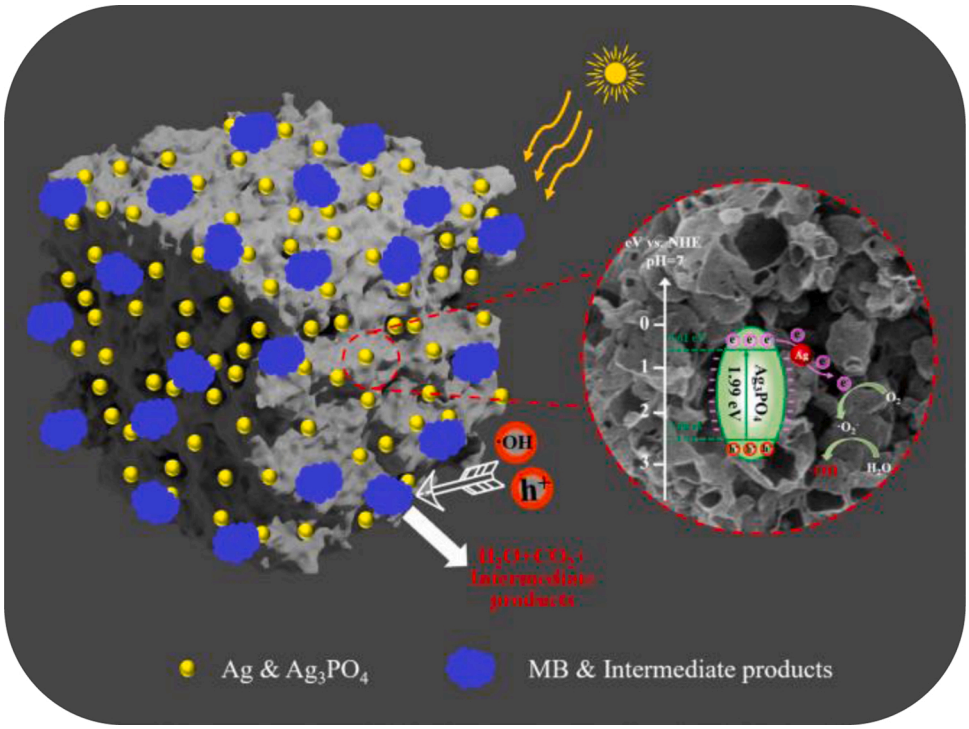

Fig. 6. Schematic illustration of MB removal mechanism of AP/PBB under visible light irradiation.

In the influence of the built-in electronic field, i.e., higher electronic density of AP and lower electronic density of PBB, the photogenerated electrons on the CB of AP are smoothly transferred to the PBB with the assistance of the noble Ag bridge. The effect of electrostatic attraction accelerates the separation of photogenerated carries and suppresses photocorrosion of AP. (3) The support PBB owing to its large specific surface area and abundant pore structure can well adsorb MB pollutant and oxygen-containing species, and then the photogenerated electrons attack to the surface adsorbed oxygen species on PBB to produce more ·OH active radicals. (4) The ·OH radicals effectively oxidized the adsorbed MB pollutant to CO_2 and H_2O.

Therefore, due to the advantages of PBB, both the adsorption and photocatalytic oxidation sites are in PBB, and thus the two-in-one effect can dramatically facilitate the overall efficient removal of MB.

4. Conclusions

In summary, a synthesis of PBB with large surface area and rich pore was developed to combine Ag_3PO_4 particles for the first time. The as-synthesized AP/PBB sample displayed remarkable removal efficiency for MB due to efficient adsorption-photocatalytic abilities. The PBB is helpful for some metallic Ag and built-in electronic field formation, visible light absorption, photogenerated charge transfer, and active free radical species, and thus led to both of the adsorption and photocatalytic oxidation site on PBB. Findings of this study revealed that AP/PBB hybrid photocatalyst has considerable application prospects in water purification, especially with respect to the removal of organic pollutants from water. Furthermore, the innovative synthesis is feasible and promising for preparing other high efficiency PBC/photocatalyst composites.

CRediT authorship contribution statement

Weixin Zou, **Bin Gao** and **Lin Dong** proposed the research and supervised the project, **Xiaoqian Wei** and **Fang Yu** designed and conducted the experiments and analyzed the experimental results, **Jinsheng Huang**, **Yue Zhang** and **Yicheng Yang** synthesized the target biochar-based photocatalysts, **Jiawei Ji**, **Yandi Cai** and **Yulin Zheng** performed the physicochemical and photochemical characterization of as-synthesized materials, **Mu. Naushad** organized data, including research literature and drawing, **Xiaoqian Wei** and **Fang Yu** wrote the manuscript, All authors discussed the results and commented on the manuscript.

Declaration of Competing Interest

The authors declare that they have no known competing financial interests or personal relationships that could have appeared to influence the work reported in this paper.

Acknowledgements

Weixin Zou, Lin Dong and Mu. Naushad would like to acknowledge the support of the National Natural Science Foundation of China (21972062), Fundamental Research Funds for the Central Universities (21114380163) and Researchers Supporting Project number (RSP-

2021/8), King Saud University, Riyadh, Saudi Arabia.

Appendix A. Supporting information

Supplementary data associated with this article can be found in the online version at doi:10.1016/j.jece.2021.106753.

References

[1] M. Wang, J. Ioccozia, L. Sun, C. Lin, Z. Lin, Inorganic-modified semiconductor TiO_2 nanotube arrays for photocatalysis, Energy Environ. Sci. 7 (7) (2014) 2182–2202, https://doi.org/10.1039/C4EE00147H.

[2] W. Lei, T. Zhang, L. Gu, P. Liu, J.A. Rodriguez, G. Liu, M. Liu, Surface-structure sensitivity of CeO_2 nanocrystals in photocatalysis and enhancing the reactivity with nanogold, ACS Catal. 5 (7) (2015) 4385–4393, https://doi.org/10.1021/acscatal.5b00620.

[3] X. Wei, X. Wang, B. Gao, W. Zou, L. Dong, Facile ball-milling synthesis of cuo/biochar nanocomposites for efficient removal of reactive Red 120, ACS Omega 5 (11) (2020) 5748–5755, https://doi.org/10.1021/acsomega.9b03787.

[4] M.M. Mian, G. Liu, Recent progress in biochar-supported photocatalysts: synthesis, role of biochar, and applications, RSC Adv. 8 (26) (2018) 14237–14248, https://doi.org/10.1039/C8RA02258E.

[5] G. Fang, J. Gao, C. Liu, D.D. Dionysiou, Y. Wang, D. Zhou, Key role of persistent free radicals in hydrogen peroxide activation by biochar: implications to organic contaminant degradation, Environ. Sci. Technol. 48 (3) (2014) 1902–1910, https://doi.org/10.1021/es4048126.

[6] Q. Chen, J. Zheng, L. Zheng, Z. Dang, L. Zhang, Classical theory and electron-scale view of exceptional Cd(II) adsorption onto mesoporous cellulose biochar via experimental analysis coupled with DFT calculations, Chem. Eng. J. 350 (2018) 1000–1009, https://doi.org/10.1016/j.cej.2018.06.054.

[7] D. Saha, S. Barakat, S.E. Van Bramer, K.A. Nelson, D.K. Hensley, J. Chen, Noncompetitive and competitive adsorption of heavy metals in sulfur-functionalized ordered mesoporous carbon, ACS Appl. Mater. Interfaces 8 (49) (2016) 34132–34142, https://doi.org/10.1021/acsami.6b12190.

[8] S. Ye, M. Yan, X. Tan, J. Liang, G. Zeng, H. Wu, B. Song, C. Zhou, Y. Yang, H. Wang, Facile assembled biochar-based nanocomposite with improved graphitization for efficient photocatalytic activity driven by visible light, Appl. Catal. B Environ. 250 (2019) 78–88, https://doi.org/10.1016/j.apcatb.2019.03.004.

[9] L. Sun, C. Tian, M. Li, X. Meng, L. Wang, R. Wang, J. Yin, H. Fu, From coconut shell to porous graphene-like nanosheets for high-power supercapacitors, J. Mater. Chem. A 1 (21) (2013) 6462–6470, https://doi.org/10.1039/C3TA10897J.

[10] K. Yang, J. Peng, C. Srinivasakannan, L. Zhang, H. Xia, X. Duan, Preparation of high surface area activated carbon from coconut shells using microwave heating, Bioresour. Technol. 101 (15) (2010) 6163–6169, https://doi.org/10.1016/j.biortech.2010.03.001.

[11] M. Armandi, B. Bonelli, F. Geobaldo, E. Garrone, Nanoporous carbon materials obtained by sucrose carbonization in the presence of KOH, Microporous Mesoporous Mater. 132 (3) (2010) 414–420, https://doi.org/10.1016/j.micromeso.2010.03.021.

[12] C. Liang, Z. Li, S. Dai, Mesoporous carbon materials: synthesis and modification, Angew. Chem. Int. Ed. 47 (20) (2008) 3696–3717, https://doi.org/10.1002/anie.200702046.

[13] T. Yan, J. Tian, W. Guan, Z. Qiao, W. Li, J. You, B. Huang, Ultra-low loading of Ag_3PO_4 on hierarchical In_2S_3 microspheres to improve the photocatalytic performance: the cocatalytic effect of Ag and Ag_3PO_4, Appl. Catal. B Environ. 202 (2017) 84–94, https://doi.org/10.1016/j.apcatb.2016.09.017.

[14] Z. Yi, J. Ye, N. Kikugawa, T. Kako, S. Ouyang, H. Stuart-Williams, H. Yang, J. Cao, W. Luo, Z. Li, Y. Liu, R.L. Withers, An orthophosphate semiconductor with photooxidation properties under visible-light irradiation, Nat. Mater. 9 (7) (2010) 559–564, https://doi.org/10.1038/NMAT2780.

[15] W.C. Peng, X. Wang, X.Y. Li, The synergetic effect of MoS_2 and graphene on Ag_3PO_4 for its ultra-enhanced photocatalytic activity in phenol degradation under visible light, Nanoscale 6 (14) (2014) 8311–8317, https://doi.org/10.1039/C4NR01654H.

[16] L. Liu, Y. Qi, J. Lu, S. Lin, W. An, Y. Liang, W. Cui, A stable Ag_3PO_4@g-C_3N_4 hybrid core@shell composite with enhanced visible light photocatalytic degradation, Appl. Catal. B Environ. 183 (2016) 133–141, https://doi.org/10.1016/j.apcatb.2015.10.035.

[17] Y. He, L. Zhang, B. Teng, M. Fan, New application of Z-scheme Ag_3PO_4/g-C_3N_4 composite in converting CO_2 to fuel, Environ. Sci. Technol. 49 (1) (2015) 649–656, https://doi.org/10.1021/es5046309.

[18] J. Liu, X. Fu, S. Chen, Y. Zhu, Electronic structure and optical properties of Ag_3PO_4 photocatalyst calculated by hybrid density functional method, Appl. Phys. Lett. 99 (19) (2011) 191903–191905, https://doi.org/10.1063/1.3660319.

[19] C. Du, Z. Zhang, G. Yu, H. Wu, H. Chen, L. Zhou, Y. Zhang, Y. Su, S. Tan, L. Yang, J. Song, S. Wang, A review of metal organic framework (MOFs)-based materials for antibiotics removal via adsorption and photocatalysis, Chemosphere 272 (2021) 1295014–1295031, https://doi.org/10.1016/j.chemosphere.2020.129501.

[20] Q. Xiang, D. Lang, T. Shen, F. Liu, Graphene-modified nanosized Ag_3PO_4 photocatalysts for enhanced visible-light photocatalytic activity and stability, Appl. Catal. B Environ. 162 (2015) 196–203, https://doi.org/10.1016/j.apcatb.2014.06.051.

[21] H. Zhang, H. Huang, H. Ming, H. Li, L. Zhang, Y. Liu, Z. Kang, Carbon quantum dots/Ag_3PO_4 complex photocatalysts with enhanced photocatalytic activity and stability under visible light, J. Mater. Chem. 22 (21) (2012) 10501–10506, https://doi.org/10.1039/C2JM30703K.

[22] X.Q. Liu, W.J. Chen, H. Jiang, Facile synthesis of Ag/Ag_3PO_4/AMB composite with improved photocatalytic performance, Chem. Eng. J. 308 (2017) 889–896, https://doi.org/10.1016/j.cej.2016.09.125.

[23] K. Talukdar, B.M. Jun, Y. Yoon, Y. Kim, A. Fayyaz, C.M. Park, Novel Z-scheme Ag_3PO_4/Fe_3O_4-activated biochar photocatalyst with enhanced visible-light catalytic performance toward degradation of bisphenol A, J. Hazard Mater. 398 (2020) 123025–123034, https://doi.org/10.1016/j.jhazmat.2020.123025.

[24] M. Tang, Y. Ao, C. Wang, P. Wang, Facile synthesis of dual Z-scheme g-C_3N_4/Ag_3PO_4/AgI composite photocatalysts with enhanced performance for the degradation of a typical neonicotinoid pesticide, Appl. Catal. B Environ. 268 (2020) 118395–118405, https://doi.org/10.1016/j.apcatb.2019.118395.

[25] D. Wang, Y. Ao, P. Wang, Effective inactivation of Microcystis aeruginosa by a novel Z-scheme composite photocatalyst under visible light irradiation, Sci. Total Environ. 746 (2020) 141149–141159, https://doi.org/10.1016/j.scitotenv.2020.141149.

[26] M. Tang, Y. Ao, C. Wang, P. Wang, Rationally constructing of a novel dual Z-scheme composite photocatalyst with significantly enhanced performance for neonicotinoid degradation under visible light irradiation, Appl. Catal. B Environ. 270 (2020) 118918–118928, https://doi.org/10.1016/j.apcatb.2020.118918.

[27] F. Rouquerol, J. Rouquerol, K. Sing, Adsorption by Powders and Porous Solids: Principles, Methodology and Applications, Academic Press, London, 1999.

[28] L. Liu, L. Ding, Y. Liu, W. An, S. Lin, Y. Liang, W. Cui, A stable Ag_3PO_4@PANI core@shell hybrid: enrichment photocatalytic degradation with π-π conjugation, Appl. Catal. B Environ. 201 (2017) 92–104, https://doi.org/10.1016/j.apcatb.2016.08.005.

[29] J.M. Saquing, Y.H. Yu, P.C. Chiu, Wood-derived black carbon (Biochar) as a microbial electron donor and acceptor, Environ. Sci. Technol. Lett. 3 (2) (2016) 62–66, https://doi.org/10.1021/acs.estlett.5b00354.

[30] M. Ren, Y. Ao, P. Wang, C. Wang, Construction of silver/graphitic-C_3N_4/bismuth tantalate Z-scheme photocatalyst with enhanced visible-light-driven performance for sulfamethoxazole degradation, Chem. Eng. J. 378 (2019) 122122–122131, https://doi.org/10.1016/j.cej.2019.122122.

[31] Y. Lin, C. Yang, S. Wu, X. Li, Y. Chen, W.L. Yang, Construction of built-in electric field within silver phosphate photocatalyst for enhanced removal of recalcitrant organic pollutants, Adv. Funct. Mater. 30 (38) (2020) 2002918–2002930, https://doi.org/10.1002/adfm.202002918.

[32] W. Zou, Y. Shao, Y. Pu, Y. Luo, J. Sun, K. Ma, C. Tang, F. Gao, L. Dong, Enhanced visible light photocatalytic hydrogen evolution via cubic CeO_2 hybridized g-C_3N_4 composite, Appl. Catal. B Environ. 218 (2017) 51–59, https://doi.org/10.1016/j.apcatb.2017.03.085.

[33] Y. Zhai, Y. Dai, J. Guo, L. Zhou, M. Chen, H. Yang, L. Peng, Novel biochar@$CoFe_2O_4$/Ag_3PO_4 photocatalysts for highly efficient degradation of bisphenol a under visible-light irradiation, J. Colloid Interface Sci. 560 (2020) 111–121, https://doi.org/10.1016/j.jcis.2019.08.065.

[34] M. Jourshabani, Z. Shariatinia, A. Badiei, Facile one-pot synthesis of cerium oxide/sulfur-doped graphitic carbon nitride (g-C_3N_4) as efficient nanophotocatalysts under visible light irradiation, J. Colloid Interface Sci. 507 (2017) 59–73, https://doi.org/10.1016/j.jcis.2017.07.106.

[35] P. Meŕel, M. Tabbal, M. Chaker, S. Moisa, J. Margot, Direct evaluation of the sp^3 content in diamond-like-carbon films by XPS, Appl. Surf. Sci. 136 (1–2) (1998) 105–110, https://doi.org/10.1016/S0169-4332(98)00319-5.

[36] Q. Li, Y. Hou, J. Wang, Y. Liu, N. Xiang, Z. Huang, Superiority of raw biomass and potassium hydroxide in preparation of ultrahigh nitrogen doping of carbon for NH_3-SCR reaction, ACS Sustain. Chem. Eng. 8 (30) (2020) 11308–11316, https://doi.org/10.1021/acssuschemeng.0c03193.

[37] X. Shi, Y. Yu, Q. Yang, X. Hong, Carboxyl groups as active sites for H_2O_2 decomposition in photodegradation over graphene oxide/polythiophene composites, Appl. Surf. Sci. 524 (2020) 146397–146406, https://doi.org/10.1016/j.apsusc.2020.146397.

[38] S. Zhou, Y. Wang, K. Zhou, D. Ba, Y. Ao, P. Wang, In-situ construction of Z-scheme g-C_3N_4/WO_3 composite with enhanced visible-light responsive performance for nitenpyram degradation, Chin. Chem. Lett. 32 (2021) 2179–2182, https://doi.org/10.1016/j.cclet.2020.12.002.

[39] N. Chen, Y. Huang, X. Hou, Z. Ai, L. Zhang, Photochemistry of hydrochar: reactive oxygen species generation and sulfadimidine degradation, Environ. Sci. Technol. 51 (19) (2017) 11278–11287, https://doi.org/10.1021/acs.est.7b02740.

[40] J. Martin, L. Nyadong, C. Ducati, M. Manley-Harris, A. Marshall, M. Kraft, Nanostructure of gasification charcoal (biochar), Environ. Sci. Technol. 53 (7) (2019) 3538–3546, https://doi.org/10.1021/acs.est.8b06861.

[41] J. Durig, G. Guirgisb, Y. Jin, Raman and infrared spectra, conformational stability, vibrational assignment and ab initio calculations of but-2-enoyl fluoride, J. Mol. Struct. 379 (1–3) (1996) 151–170, https://doi.org/10.1016/0022-2860(95)09149-1.

[42] Y. Kuang, J. Shang, T. Zhu, Photoactivated Graphene Oxide to Enhance Photocatalytic Reduction of CO_2, ACS Appl. Mater. Interfaces 12 (3) (2020) 3580–3591, https://doi.org/10.1021/acsami.9b18899.

[43] C. Chen, H. Zeng, M. Yi, G. Xiao, S. Xu, S. Shen, B. Feng, In-situ growth of Ag_3PO_4 on calcined Zn-Al layered double hydroxides for enhanced photocatalytic degradation of tetracycline under simulated solar light irradiation and toxicity assessment, Appl. Catal. B Environ. 252 (2019) 47–54, https://doi.org/10.1016/j.apcatb.2019.03.083.